Anion Effects in the Scattering of CO2 from the Room-Temperature Ionic Liquids [bmim][BF4] and [bmim][Tf2N]: Insights from Quantum Mechanics/Molecular Mechanics Trajectories

3 AUTHORS, INCLUDING:

Xiaohu Li
Sandia National Laboratories
15 PUBLICATIONS   **138** CITATIONS

SEE PROFILE

Anion Effects in the Scattering of CO_2 from the Room-Temperature Ionic Liquids [bmim][BF4] and [bmim][Tf2N]: Insights from Quantum Mechanics/Molecular Mechanics Trajectories

Xiaohu Li,[†] George C. Schatz,*[,†] and David J. Nesbitt*[,‡]

[†]Department of Chemistry, Northwestern University, 2145 Sheridan Road, Evanston, Illinois 60208-3113, United States
[‡]JILA, Campus Box 440, University of Colorado, Boulder, Colorado 80309-0440, United States

Ⓢ *Supporting Information*

ABSTRACT: Quantum mechanics/molecular mechanics (QM/MM) molecular dynamics simulations have been carried out to model the scattering of hyperthermal (15 kcal/mol) CO_2 on the surfaces of two common imidazolium based room-temperature ionic liquids (RTILs) [bmim][BF4] and [bmim]-[Tf2N]. Good agreement was achieved in comparison with experiment. The [bmim][BF4] surface is found to be more absorptive of CO_2 than [bmim][Tf2N], which leads to greater loss in translational energy and less rotational excitation of CO_2's that scatter from [bmim][BF4]. These differences are found to result from a interplay of differences in the structure of the interface and the strength of interactions that depend on anion identity. Our results also suggest that CO_2 interacts strongly with ionic species on the RTIL surfaces due to the large induced dipole moments on CO_2 during the collisions. The inclusion of electronic polarization is critical in determining the final rotational excitation of CO_2 compared to results from an MM model with fixed charge.
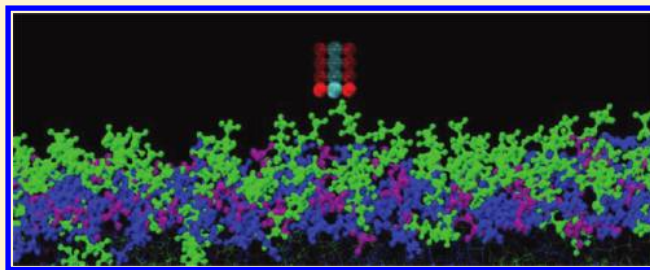
1. INTRODUCTION

The properties of gas/condensed phase interfaces play a vital role in materials, atmospheric, and biological chemistry. For example, the question of whether water is acidic or basic at the air–water interface has been debated over the past decade.[1−7] Lack of understanding of interfaces is especially important for room-temperature ionic liquids (RTILs), which are salts with melting points below 100 °C. Their low volatility, low viscosity, high chemical and thermal stability, and large structural diversity for tuning of properties have led to applications in a wide variety of areas, providing motivation to provide better descriptions of interfacial properties. Applications of RTILs include replacement of volatile organic solvents and dipolar aprotic solvents,[8,9] multiphase catalysis,[10] flue gas emission control,[11−13] extraction,[10,11] hydrogen fuel cells,[14] solvents for nuclear fuel processing[15] and cellulose processing,[16] substrates for depositing surface-enhanced Raman scattering active nanoparticles,[17] and heat transfer media in solar thermal energy systems.[18] In addition, RTILs have been considered as possible propellants in cone-jets and as environmentally benign hypergolic bipropellants.[19−23]

The characterization of RTIL surfaces requires understanding many properties (e.g., surface topology, electronic polarization of various ionic species, charge redistribution, influence of the bulk properties, effects of impurities, and so forth), and there have been many recent measurements in this direction. Ouchi et al.[24−28] have used sum-frequency generation (SFG) vibrational spectroscopy to probe the surfaces of several

alkylimidazolium-based RTILs as well as binary mixtures of RTILs and water. In general, the surface of RTILs is shared between cations and anions with the alkyl chain on the cation ring aligned nearly parallel to the surface normal. In addition, these studies also indicate surface enhancement of cations when the bulk RTIL concentration reaches the submillimolar level in mixtures composed of the RTIL and water. In contrast, aqueous solutions of various inorganic electrolytes show anion enhancements at very low concentrations.[2,29] Baldelli et al.[30−34] have probed the surface properties of various RTILs composed of alkylimidazolium cations paired with a series of anions using SFG vibrational spectroscopy. Similar conclusions have been reached concerning the composition of the surface and orientation of the alkyl chains. Furthermore, they find that the imidazolium ring lies flat on the surface. Water effects on the orientation of cations and anions were also studied. As water vapor is increased, the cation rings tend to be oriented at a tilt angle on the surface. Contrary to the SFG experiments, ion recoil mass spectroscopy showed that the butyl chains lie flat on the surface in [bmim][PF6].[35] An alternative yet powerful way to explore the composition of RTIL surface is by molecular beam scattering, which has been widely used to probe the interfacial properties of condensed matter media.[36] McKendrick and co-workers used laser-induced fluorescence to

probe the OH products resulting from low energy reactive $O(^3P)$ radical scattering on $[Cnmim][Tf2N](n = 2, 4, 5, 8, 12)$. Evidence has been found to support the alkyl abundance on RTIL surfaces with longer alkyl chains. Roscioli and Nesbitt probed the ro-vibrational states of inelastically scattered CO_2 on a series of $[Cnmim][BF4]$ and $[Cnmim][Tf2N]$ surfaces ($n = 2, 4, 6, 8, 12$). In addition to the alkyl abundance for longer alkyl chains, they also observed an anion effect on the surface with $[Tf2N]$.[37,38]

Theoretical simulations have been used to provide useful insights concerning vacuum−RTIL interfacial properties. Molecular dynamics (MD) simulations for alkylimidazolium-based liquids with both polarizable and nonpolarizable force fields[39−45] show that there is a maximum density region along the surface normal beneath the outermost region of the interface. This is because the imidazolium rings prefer to be aligned along the surface normal in the maximum density region, and then the alkyl chains produce a lower density region at the interface. The orientations of the alkylimidazolium rings and alkyl chains on the interface agree with most experimental results, and theory also shows that surface ordering is affected by anion identify, i.e., in the anion $[Tf2N]$-based RTILs, similar to the alkyl chain, the terminal trifluoromethyl (CF_3) group of $[Tf2N]$ protrudes away from the surface into vacuum.[45]

In addition to the vacuum−liquid results, many experimental and simulation studies have focused on surface physisorption and bulk dissolution of CO_2 into RTILs. While CO_2 is highly soluble in RTILs, RTILs are virtually insoluble in CO_2. This phenomenon allows very efficient extraction of products by supercritical CO_2 from the catalytically active RTIL phase. In the interplay of supercritical CO_2 and RTILs lies great potential for carbon sequestration, product extraction, and enzyme catalysis.[10,11] These results have stimulated efforts in unraveling the interactions between CO_2 and RTILs. Brennecke et al.[46] measured the solubility of CO_2 in various RTILs and concluded that CO_2 solubility strongly depends on anion identity, with the $[Tf2N]$-based RTILs showing the highest CO_2 solubility. Welton et al.[47] utilized attenuated total reflectance infrared (ATR-IR) spectroscopy to investigate the bending mode of CO_2 dissolved in $[bmim][PF6]$ and $[bmim][BF4]$. On the basis of the splitting of the bending vibration, they found a weak Lewis acid−base-type interaction between CO_2 and the anions. Roscioli and Nesbitt[38] studied the quantum-resolved ro-vibrational states of CO_2 molecules that were scattered off surfaces of the RTILs $[bmim][BF4]$ and $[bmim][Tf2N]$. An analysis based on a trapping-desorption/impulsive scattering (TD/IS) model showed strong dependence of the final rotational energy in the IS channel and also in the trapping fraction on anion identity.

In theoretical studies of biphasic mixtures of CO_2 interacting with ionic liquids, Maginn and co-workers[48] have utilized MD methods to show that there is strong CO_2 organization about the anions. Surface adsorption and subsequent dissolution of CO_2 in RTILs were also explored, and Perez-Blanco et al.[49] found a dense layer of adsorbed gas-phase CO_2 on the RTIL interface for various CO_2 pressures. Several gas-phase *ab initio* cluster models of CO_2 and RTILs (with stationary optimization calculations) using DFT BLYP displayed Lewis acid−base-type interaction between CO_2 and the anions.[50,51] Since there are strong interactions with the anions, the CO_2 prefers a distorted geometry and thus possesses a significant induced dipole. This phenomenon is also confirmed in Car−Parrinello MD simulations of a mixture of CO_2 and bulk RTILs using density

functional theory (DFT) BLYP calculations under periodic boundary conditions (PBC).[52]

Despite these pioneering studies, there are several gaps that have not been filled in as follows: (1) most of the adsorption and dissolution simulations of CO_2 in RTILs have utilized a classical point charge force field model, whereas it has been found that the dipole−induced-dipole interaction is important when CO_2 approaches the anion;[50−52] (2) due to the enormous computational requirements of ab initio MD simulations, it is only possible to treat a rather limited number of ion pairs, while the gas−RTIL interface is only well-defined with a reasonable number of ion pairs; (3) the lack of direct comparison between simulations and experiments makes it difficult to decipher the critical factors governing the interaction between CO_2 and RTIL surfaces. In this publication, we address the above issues by mixed quantum mechanics/molecular mechanics (QM/MM) MD calculations. The system we have studied involves hyperthermal gaseous CO_2 scattering from the surface of $[bmim][BF4]$ or $[bmim][Tf2N]$ (see Figure 1 for chemical
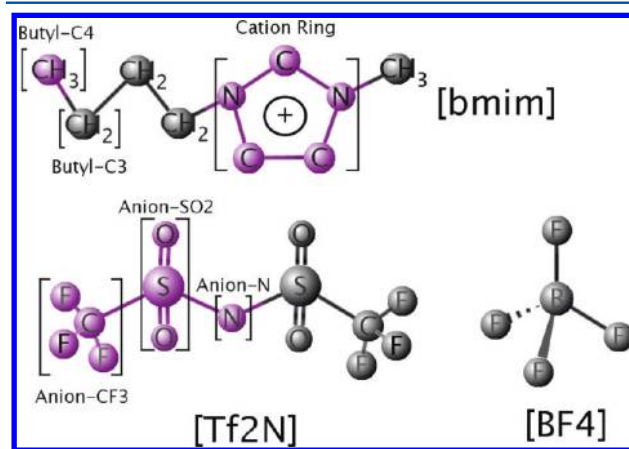

Figure 1. Chemical structures of the cation and anions of RTILs studied in this work. To facilitate discussions, the nomenclature for the different groups is shown. Groups are highlighted in purple and surrounded by enclosed brackets. Note that groups with identical stoichiometry are not repeated.

structures). These QM/MM MD calculations enable us to simulate the interaction between CO_2 and RTIL using a force field that includes electronic polarization effects. Furthermore, we are able to present a detailed investigation of the anion dependence of the CO_2 interaction with $[bmim][BF4]$ and $[bmim][Tf2N]$, which reveals and explains the experimentally observed differences between the two liquids.

This paper is organized as follows: In Section 2, details of the QM/MM MD method are first presented. The semiempirical PM6[53] method with dispersion and hydrogen bonding corrections[54,55] was adopted for the electronic structure calculation. In Section 3.1, we report the structural properties of $[bmim][BF4]$ and $[bmim][Tf2N]$ from MD simulations using slab boundary conditions (SBC). The final CO_2 states from simulations of the scattering experiments are characterized in terms of translational, rotational, and vibrational energy transfer in Section 3.2. The key factors responsible for the difference between $[bmim][BF4]$ and $[bmim][Tf2N]$ are analyzed in detail in Section 3.3, with reasonable agreement between simulation and experiments. In addition, scattering results in which a classical force field (rather than QM/MM forces) is used are presented in Section 3.4. The TD fraction

3588

dx.doi.org/10.1021/jp2123357 | J. Phys. Chem. B 2012, 116, 3587–3602

and IS channel rotational temperature obtained from both QM/MM and MM results are also presented and directly compared with experimental findings. Finally, we summarize our conclusions in Section 4.

2. METHODOLOGY

2.1. Generation of Interfaces. To generate interfaces for scattering gaseous CO_2 from the RTIL surface, the following procedure was used. First, for each RTIL chosen, 640 ion pairs were placed randomly in a rectangular box. Following a 500 ps equilibration at 298 K using Berendsen's isothermal–isobaric (NPT) ensemble,[56] another 4 ns production NPT was run at 298 K and 1 atm using a Nose–Hoover[57,58] thermostat and Martyna's implementation[59] for pressure control. Throughout this work, the all-atom OPLS-AA type force field was utilized.[60] This force field has been optimized for the modeling of common RTILs. In all MD simulations, a time step of 0.8 fs, a nonbonded cutoff distance of 15 Å with appropriate tail correction, particle-mesh Ewald (PME) for long-range Coulomb forces, and PBC were adopted. The bulk mass densities of both RTILs, [bmim][BF4] and [bmim][Tf2N], are in good agreement with experiments, as indicated in Table 1.

Table 1. Details of MD Calculations Using SBCs

	[bmim][BF4]	[bmim][Tf2N]
number of ion pairs	640	640
temperature (K)	298	298
production run (ns)	4.0	4.0
bulk density (g/cm^3)	1.14 (1.20^a)	1.43 (1.43^b)
cell dimensions x, y, z (Å)	64.6, 76.0, 120.0	82.9, 76.6, 150.0

^{a}Experimental value from ref 61. ^{b}Experimental value from ref 62.

The final geometries from these NPT runs were plucked out, and SBC was applied by increasing the z dimension of the cell. NVT-simulated annealing from 400 to 298 K over a 800 ps period with a Nose–Hoover thermostat was first carried out, followed by another 4 ns NVT production run at 298 K. Simulations were performed using version 4.5.3 of GRO-MACS.[63] Details of the simulations are summarized in Table 1.

2.2. QM/MM MD Trajectories. From the previous SBC simulation, 50 structures were selected for each RTIL. Between 8 and 32 spots on the surface of each structure were randomly picked and chosen as the QM region along with nearby ion pairs based on distance criteria. A CO_2 molecule was then placed 10 Å above the surface at the top of the QM region and was directed toward the surface with a translational energy of 15 kcal/mol (at an incoming polar angle $\theta_i = 0$ or 45°). The initial vibrational energy was sampled using a Maxwellian

distribution of 200 K with rigid body rotation projected out. The chosen initial vibrational temperature was based on an estimate from the previous experiment in ref 36m. The surface slab was given an initial Maxwellian kinetic energy at 298 K. The resultant QM region is composed of 10 and 7 ion pairs plus CO_2 in [bmim][BF4] and [bmim][Tf2N] with a radius ranging from 15 to 20 Å. Mechanical embedding[64] is utilized for the QM/MM interaction. The dynamics were integrated using a time-reversible velocity verlet algorithm[65,66] with time step of 0.8 fs and microcanonical ensemble (NVE). During the course of dynamics, the temperature of the slab maintains ambient conditions. The trajectory was terminated whenever CO_2 left the surface for at least 10 Å or the dynamics reached 12 ps. The typical total energy drift per atom is on the order of 10^{-7} kcal/mol. QM/MM MD calculations were performed using a modified version of GROMACS 4.5.3 interfaced with MOPAC 2009.[67] The EPM-2 (elementary physical model) was used to describe the intermolecular interaction of CO_2 with the RTILs,[68] and the bond and bending force constants for CO_2 from ref 69 were utilized for the MM scattering simulations as presented in Section 3.4. We note that the bond and angle force constants from ref 69 reproduce the vibrational frequencies of gas-phase CO_2. Parameters of the MM force field for CO_2 are provided in the Supporting Information. A summary of the QM/MM MD trajectory calculations is given in Table 2.

Since thousands of scattering trajectories are needed to obtain a reasonable statistical average, we have chosen PM6[53] with dispersion and hydrogen bonding corrections (PM6-DH)[54,55] as the electronic structure method. The justification of this method is presented in the next section, where we have shown that PM6-DH is reasonably accurate compared to DFT B3LYP with dispersion correction[70] and MP2.

2.3. Choice of Electronic Structure Theory. In order to accurately account for the interaction of CO_2 with the chosen RTILs, we have utilized the NNDO-type semiempirical method PM6.[53] The PM6 method has been substantially improved over PM3 in describing equilibrium geometries and heats of formation over extensive sets of systems. Furthermore, dispersion and hydrogen bonding corrections[54,55] were developed for this semiempirical method. The PM6-DH method has been demonstrated to achieve accuracy comparable with DFT for inorganic, organic, and biological systems.[53–55] In this section, we benchmarked the PM6-DH method by studying the binding energy of CO_2 with the cation [bmim] and anions [BF4] and [Tf2N]. Here PM6-DH results are compared to B3LYP with dispersion correction (B3LYP-D) and post-Hartree–Fock MP2. In addition, results obtained from MM(fixed charge)

Table 2. Simulation Parameters of QM/MM MD

	[bmim][BF4]		[bmim][Tf2N]	
	$\theta_i = 0°$	$\theta_i = 45°$	$\theta_i = 0°$	$\theta_i = 45°$
no. of total trajectories	1608	1020	800	800
no. of atoms in QM region	303		283	
total energy drift^a (kcal·mol^{-1}·atom^{-1})	1.7×10^{-7}	5.6×10^{-7}	1.4×10^{-7}	1.3×10^{-7}
temperature of slab^b (K)	300.8	300.7	297.2	300.8
ensemble	microcanonical (NVE)			
CO_2 initial translational energy (kcal/mol)	15			
CO_2 initial vibrational energy	Maxwellian at 200 K			

^{a}Averaged over 400 trajectories. ^{b}Averaged over 400 trajectories, with CO_2 excluded.

Table 3. Binding Energies of CO$_2$ with Cation and Anions

	binding site	PM6	PM6-DH	B3LYP[a]	B3LYP-D[c]	MP2[a,b]	MM
					(kcal/mol)		
[bmim]	cation ring	−0.33	−2.28	0.75	−3.46	−4.94	−2.38
	butyl-C4	0.12	−0.43	0.37	−0.69	−1.29	−2.52
[BF4]	[BF4]	−4.50	−5.31	−5.02	−7.02	−7.18	−4.44
[Tf2N]	anion-SO2	−3.87	−4.96	−2.74	−5.48	−6.36	−4.08
	anion-CF3	−4.02	−5.00	−0.84	−2.63	−3.18	−2.04
	anion-SO2	−4.03	−5.01	−2.43	−5.50	−6.18	−4.52

[a]Double zeta basis Def2-SVP[72,73] with Pople diffuse functions (d,p)[74] was used. Resolution of identity (RI)[75−78] approximation of the Coulomb integral using auxiliary basis set for Def2-SVP[75,77] and a pseudospectral approximation for the exchange integral[79] were utilized. [b]Frozen core approximation. [c]Grimme's dispersion corrections for DFT.[70]
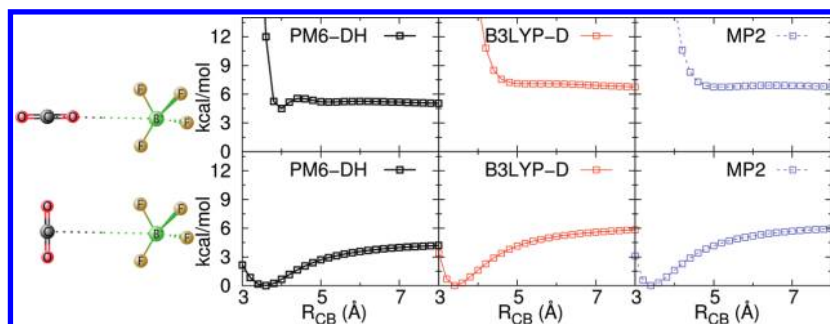

Figure 2. PES of CO$_2$ approaching the anion [BF4] with two different orientations based on the methods PM6-DH, B3LYP-D, and MP2. CO$_2$ approaches [BF4] with head-on (top panel) and flat configurations (bottom panel). The geometries of CO$_2$ and [BF4] were optimized with PM6-DH and were fixed when CO$_2$ reaches [BF4]. All results for the same level of theory were shifted according to the minima found in the flat configuration.
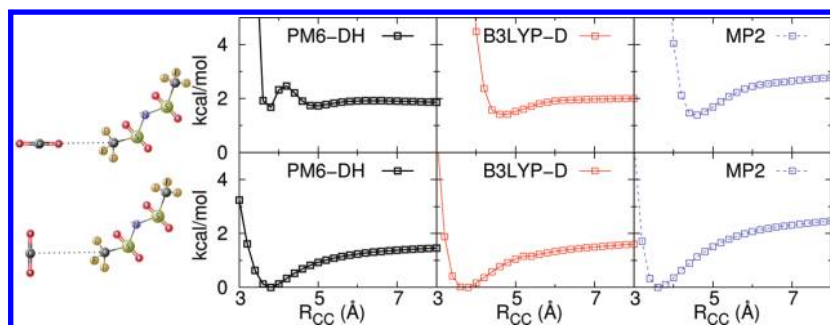

Figure 3. PES of CO$_2$ approaching the terminal CF$_3$ group in the anion [Tf2n] with two different orientations using the methods PM6-DH, B3LYP-D, and MP2. CO$_2$ approaches [Tf2N] with head-on (top panel) and flat configurations (bottom panel). The geometries of CO$_2$ and [Tf2N] were optimized with PM6-DH and were fixed when CO$_2$ reaches [Tf2N]. All results for the same level of theory were shifted according to the minima found in the flat configuration.

were also provided. The PM6-DH, ab initio, and MM calculations were done with MOPAC2009, GROMACS, and ORCA,[71] respectively. Results are summarized in Table 3.

As shown in Table 3, we have probed various configurations of CO$_2$ with both the cation [bmim] and anions [BF4] and [Tf2N]. It should be noted first that the geometrical dependence of the trend in binding energy is reproduced using both PM6 and PM6-DH compared with B3LYP, B3LYP-D and MP2. CO$_2$ interacts most strongly with [BF4], followed by [Tf2N] and [bmim]. This is consistent with previous ab initio cluster calculations.[50,51] Moreover, dispersion plays an important role in the interaction between CO$_2$ and RTILs. Both PM6-DH and B3LYP-D show improved results over uncorrected results compared to MP2. We also note that the portion of the binding energy due to dispersion is significantly larger with the bigger ions [bmim] and [Tf2N]. In comparison with MP2, the root-mean-square (rms) error of PM6-DH

across Table 3 is 1.73 kcal/mol. It should be noted that the MM results are only slightly worse than PM6-DH (rms error 2.03 kcal/mol), which is not surprising since the OPLS-AA type force field for RTILs has been well parametrized to equilibrium properties. However, the discrepancy of CO$_2$ scattering results between MM and both QM/MM and experimental data in Section 3.4 strongly suggests that the electronic polarization effect from nonequilibrium configurations during scattering is critical.

Lastly, we also benchmarked the potential energy surface (PES) of CO$_2$ interacting with the anions [BF4] and [Tf2N]. The results are provided in Figures 2 and 3. The optimized geometries of CO$_2$ and the anions were obtained separately using PM6-DH, and the geometries were fixed when CO$_2$ approaches the anions. Only the PES of CO$_2$ approaching the terminal CF$_3$ group of [Tf2N] is presented, since it is shown in Section 3.1 and Section 3.2 that this is the dominant group in

[Tf2N] responsible for the CO_2 scattering. In general, the PM6-DH results are in agreement with both B3LYP-D and MP2, especially when CO_2 approaches the anions with "flat" orientation. Furthermore, the degree of anisotropy in the PES with respect to CO_2 rotation is larger when CO_2 interacts with [BF4], as CO_2 strongly prefers the flat arrangement to a "head-on" structure. The degree of anisotropy, however, is greatly reduced in the interaction of CO_2 with the CF_3 in [Tf2N]. Hence, the cluster study here suggests that important differences in the degree of anisotropy in the interaction of CO_2 with the anions, and this will influence rotational excitation, as will be further probed in Section 3.3.

3. RESULTS AND DISCUSSION

3.1. Structures of Ionic Liquid Surfaces. In Figure 4, partial mass and number density profiles along the surface normal
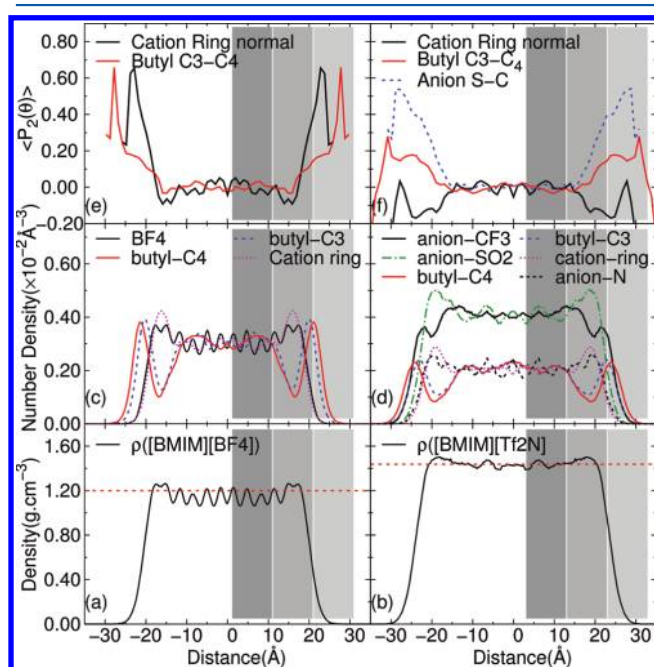

Figure 4. Mass and number density profiles along the surface normal for [bmim][BF4] (a,c) and [bmim][Tf2N] (b,d). Average second-order Legendre polynomial $\langle P_2(\theta) \rangle$ of various directional angles in [bmim][BF4] (e) and [bmim][Tf2N] (f). Gray areas depict different regions along the surface normal. From the darkest to lightest: bulk, maximum-density, and surface regions. The red dashed horizontal lines represent experimental mass density values.

(z axis) as well as the average second Legendre polynomial $\langle P_2(\theta) \rangle$ for several directional angles from both RTILs are shown. The density profile is defined as

$$\rho(V) = \frac{\sum_{Z_A \in \mathcal{R}} \int_{V-\Delta V/2}^{V+\Delta V/2} \delta(\bar{\mathbf{r}}_{Z_A} - \bar{\mathbf{r}}) M_{Z_A} d\bar{\mathbf{r}}}{\Delta V} \quad (1)$$

where Z_A is the atomic number, and $\mathcal{R}$ is a group of selected atoms. Equation 1 computes the average density of the group $\mathcal{R}$ in a unit volume ΔV around volume V. Note that M_{Z_A} is 1 when the number density is used and equals the atomic weight of atom Z_A in the case of mass density. In the one- (1D) and two-dimensional (2D)

reduced density profiles, V is mapped to the surface normal coordinates and surface area.

In order to facilitate discussion, we have designated a nomenclature for various groups in the ionic species as shown in Figure 1. We first divide the interface region into three distinct areas (gray solid areas) based on the density profiles presented in Figure 4a–d. In the surface region, the number densities of all groups decrease when approaching the vacuum side, extending over a range of 5 Å. Moving further down from the surface region, the number density approaches a maximum/minimum (depending on identity of groups) with thickness of about 10 Å. Lastly, both the number and mass densities show oscillating patterns in the bulk phase. Those regions have been noted in several experimental and theoretical studies.[39−45,80] Furthermore, we note that oscillation in the bulk is significantly reduced in [bmim][Tf2N], indicating a strong anion dependence of structural ordering.

Another distinct feature is the difference in composition of the surface region of the two RTILs (lightest gray areas in Figure 4c,d). While the [bmim][BF4] surface is dominated by the butyl chains (butyl-C3 and butyl-C4), the terminal CF_3 groups (anion-CF3) compete with the butyl chains on the [bmim][Tf2N] surface.

In Figure 4e,f, we investigated the orientations of cation and anion in both RTILs using the average second-order Legendre polynomial $\langle P_2(\theta) \rangle$. The definition is given as

$$\langle P_2(\theta) \rangle = \left\langle \frac{1}{2} (3 \cos^2 \theta - 1) \right\rangle \quad (2)$$

where θ is the directional angle of various groups with respect to the surface normal. Angles in the plot are based on the normal to the cation ring, the vector that connects butyl C3 and C4 in [bmim], and that which joins the sulfur and carbon in [Tf2N]. Those vectors represent the orientations of the cation ring, the terminal butyl chain, and the terminal anion-CF_3 groups on the surface, respectively. It is clear that the butyl chains protrude from the [bmim][BF4] surface into the vacuum (large $\langle P_2(\theta) \rangle$ value in the surface region). Meanwhile, the cation rings prefer to be aligned parallel to the surface since the angle between the ring normal and the surface normal approaches zero. In stark contrast, the ordering of ionic species on the [bmim][Tf2N] surface is drastically different. While the relatively shorter terminal anion-CF_3 groups point into the vacuum, the butyl chains are flattened. Furthermore, the cation rings lack any preferential directionality on the surface. Lastly, it should be noted that compared to [bmim][BF4], the cation rings in [bmim][Tf2N] show propensity to be aligned perpendicular to the surface in the maximum-density region.

The surface-dominant and protruding butyl chains make the surface of [bmim][BF4] rougher than that of [bmim][Tf2N], where the interface is shared between the flatter butyl chains and terminal anion-CF_3 groups. Hence, the scattering dynamics of gas molecules are expected to be different on the two surfaces due to the difference in surface topology. This aspect will be further explored in our subsequent scattering simulations in Section 3.2 and Section 3.3.

It is known that enhanced surface populations of ions will result in a decrease in surface tension.[2] The surface enhancement of anion groups in [bmim][Tf2N] therefore suggests a smaller surface tension. To verify this, we evaluated surface tension from our simulations using

$$\gamma = \frac{L_z}{2} \left(\langle \Pi_{zz} \rangle - \frac{\langle \Pi_{xx} + \Pi_{yy} \rangle}{2} \right) \quad (3)$$
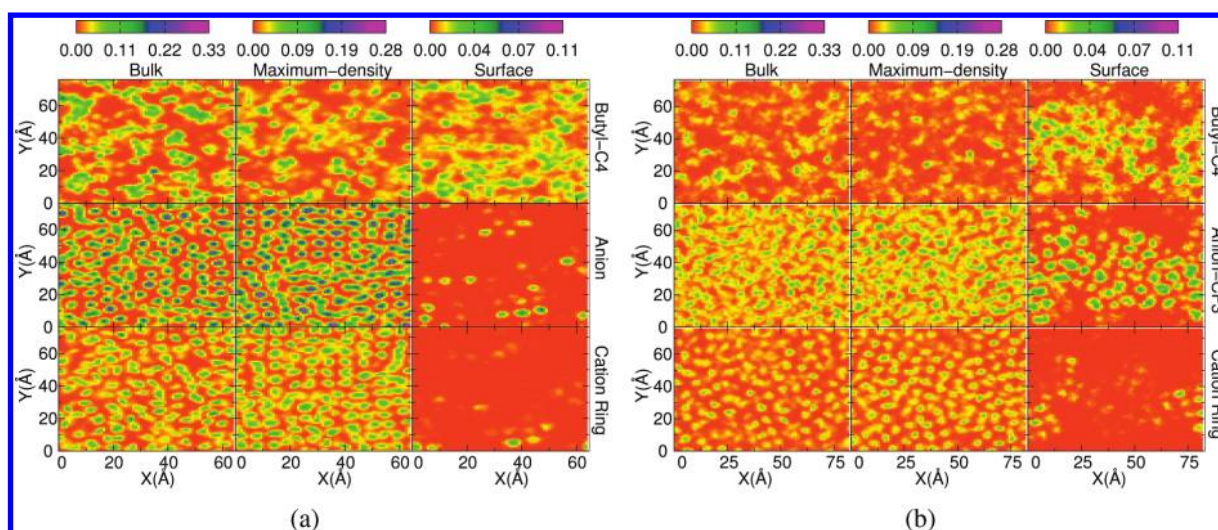
Figure 5. Looking down along the surface normal, reduced 2D number density maps of different groups of (a) [bmim][BF4] and (b) [bmim][Tf2N] in the three different regions shown in Figure 4 as shaded areas. Note that all plots have been scaled by a factor of 100, and the units are the number of sites/Å^3.
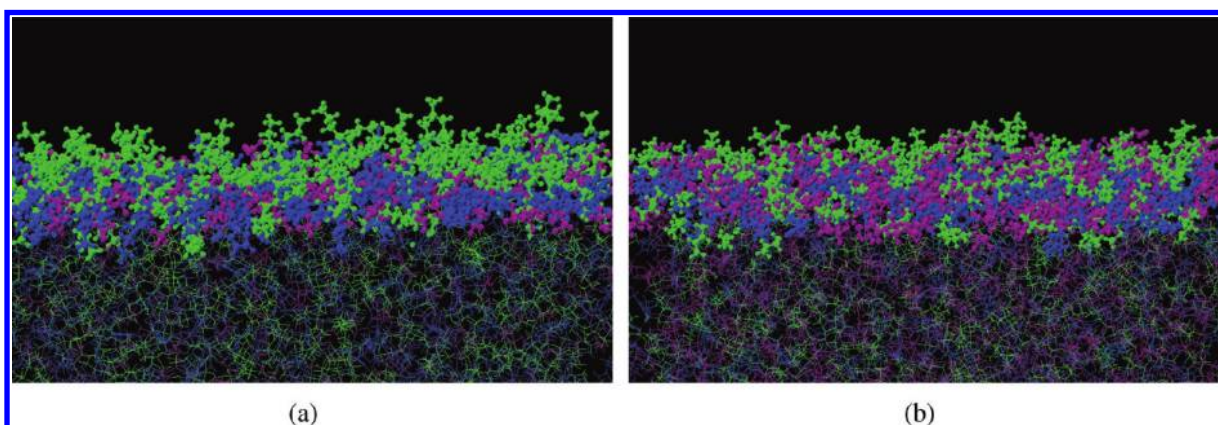

Figure 6. Side view of surface structures of [bmim][BF4] (a) and [bmim][Tf2N] (b) from the last snapshot from SBC MD simulations. The top layer of molecules is displayed using a ball−stick form, while all the others underneath are represented using lines. Note that butyl chains, cation rings, and anions are represented using green, blue, and purple colors, respectively.

where Π_{xx}, Π_{yy}, and Π_{zz} are the principal components of pressure tensor. The running average of surface tension provided in the Supporting Information seems to indicate the convergence of the surface tension. The estimated γ is 46.5 ± 10.0 mN/m for [bmim][BF4] and 33.0 ± 6.9 for mN/m for [bmim][Tf2N], in good agreement with experiments.[81−83]

To further probe the structural ordering of the two RTILs, in Figure 5 we provide a reduced 2D number density map for a few representative groups in the bulk, in the maximum-density region, and in the surface region. First and foremost, different surface orderings are evident as the butyl chains overwhelmingly occupy the [bmim][BF4] surface region with only a few scattered [BF4]. By contrast, the [bmim][Tf2N] surface is equally shared between the butyl-C4 and anion-CF3 groups. Since the gas uptake coefficient or trapping fraction at interfaces strongly depends on the interaction between gas molecules and surface dominated groups, we can deduce that the adsorption efficiency of CO_2 on the two RTILs surfaces will differ. This difference, however, will also depend on an interplay of surface roughness, the binding of CO_2 with surface enhanced groups, and the diffusion of gas molecules to the

bulk. In fact, gas/liquid scattering experiments have shown that the trapping fraction is correlated with the enthalpy of adsorption (See refs 36a, 37, and 38). We will address the difference in scattering behavior in terms of surface roughness and CO_2 binding energies with the surface enhanced groups in Section 3.3 and Section 3.4. We also note that the terminal methyl in the butyl chain is much more diffusive than other groups, as evidenced by the much broader distribution in all three regions. This of course, is directly related to the flexible nature of the butyl structure.

Snapshots of the RTIL surfaces are presented in Figure 6a,b. In both figures, the various groups are color-coded. The green, blue, and purple colors represent the butyl chains, cation rings and anions in both RTILs. It is clear that ridges are formed due to the protruding butyl chains on the [bmim][BF4] surface. In addition, the more flattened butyl chains and surface enhanced anion-CF3 make the [bmim][Tf2N] surface a smooth one.

Comparison of the surface topology of RTILs using nonpolarizable and polarizable force fields has been done by Yan et al.[44] It is found that while polarization reduces the surface tension significantly, the influence on surface topology is less severe. In summary, features of the structural topology of

the two RTIL interfaces agree with existing theoretical and experimental studies of similar RTILs. The surface tension from our simulations accurately matches experimental results. This gives us confidence to use our simulations to define the starting structures in our QM/MM MD simulations.

3.2.1. CO₂ Scattering Results. *Scattering Probability.* Results from our scattering calculations for 15 kcal/mol translational energy are summarized in Table 4. We first note

Table 4. Summary of CO₂ Scattering Results[a]

	[bmim][BF4]		[bmim][Tf2N]	
	$\theta_i = 0°$	$\theta_i = 45°$	$\theta_i = 0°$	$\theta_i = 45°$
total scattering probability	0.10	0.17	0.38	0.49
$\langle \theta_{out} \rangle (°)$	44.9	41.7	41.7	47.2
$\langle \Delta T_{trans} \rangle$	−12.9	−12.7	−12.5	−11.8
$\langle \Delta T_{rot} \rangle$	1.16	1.20	1.40	1.54
$\langle \Delta T_{vib} \rangle$	−0.16	−0.18	−0.070	−0.13
$(|\langle \Delta E_{tot} \rangle|)/T_{init}$	0.78	0.76	0.74	0.68
$\langle \Delta T_{\nu_1} \rangle$[b]	0.017	−0.0005	0.0075	0.012
$\langle \Delta T_{\nu_2} \rangle$	−0.11	−0.11	−0.022	−0.069
$\langle \Delta T_{\nu_3} \rangle$	−0.07	−0.067	−0.053	−0.072
$\langle J \rangle$[c]	27	28	29	31

[a]Energy unit is kcal/mol. All final results are averaged over a time window of 0.5 ps. [b]ν_1, ν_2, and ν_3 are the symmetric stretch, bending, and asymmetric stretch modes of CO₂, respectively. [c]Defined using the quasi-classical relation, $L = (J(J + 1))^{1/2}\hbar$, where L is the angular momentum.

that no evidence of chemical reaction has been found in our results due to the chemical stability of both CO₂ and RTILs. A trajectory was identified as scattered when the CO₂ left the surface for at least 10 Å. However, due to the finite simulation length, the scattering probability from our simulation is likely a lower bound estimate. Table 4 shows that CO₂ has a notably higher probability to be scattered off [bmim][Tf2N] than [bmim][BF4]. This reflects the difference in interaction between CO₂ and the two surfaces during the scattering process. In addition, the scattering probability generally increases with increasing incident angle. Finally, the outgoing angle of CO₂ coming off the [bmim][BF4] surface is inversely proportional to the incident angle. This trend, however, is reversed in [bmim][Tf2N]. We provide the distribution of outgoing angles in Figure 7.

3.2.2. Energy Transfer to and from CO₂. To analyze energy transfer, we have decomposed the total kinetic energy of CO₂ as

$$T_{tot} = T_{trans} + T_{rot} + T_{vib} \tag{4}$$

where T_{trans}, T_{rot}, and T_{vib} are the center-of-mass (COM) translational, body-frame rigid-body rotational and vibrational energy. In order to investigate energy transfer in the vibrational modes, the body-frame vibrational velocity was projected onto the normal modes as

$$\vec{v}_{vib}(t) = \sum_i C_i(t) \vec{H}_i \tag{5}$$

where $\vec{v}_{vib}(t)$ is the 3N-dimensional, time-dependent, mass weighted body-frame vibrational velocity vector and $\{\vec{H}_i\}$ are
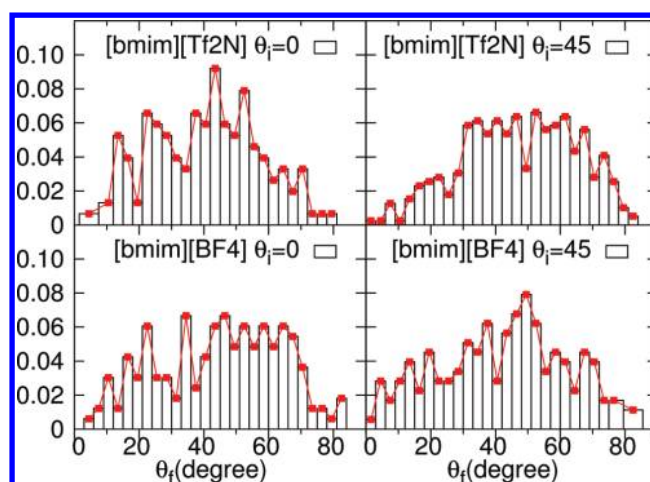

Figure 7. Angular distribution of CO₂ scattering from [bmim][BF4] and [bmim][Tf2N] at incident angles $\theta_i = 0°$ and $\theta_i = 45°$.

the orthonormal harmonic normal modes. Since $\{\vec{H}_i\}$ form a complete, orthonormal set, we obtain

$$T_{vib} = \frac{1}{2}\vec{v}_{vib}(t) \cdot \vec{v}_{vib}(t) = \sum_i \frac{1}{2}C_i^2(t) = \sum_i T_i \tag{6}$$

where T_i is the kinetic energy in normal mode $\vec{H}_i$. Hence, eq 5 allows us to probe the energy flow in each vibrational mode, with the change in translational energy associated with a given vibration expected to be approximately half the change in total vibrational energy for that mode. This method was previously adopted to study vibrational energy transfer in hydrogen-bonded ionic clusters.[84,85]

Table 4 presents average energy transfer results for both liquids and incident angles, where only nontrapped trajectories are used to calculate the results. All the probability distributions of energy transfer in translational, rotational, and vibrational degrees of freedom are presented in Figure 8. The table shows that nearly 80% of the initial translational energy is lost to the surfaces in these collisions. In addition, both the translational energy loss and the portion of energy transferred to the surface are higher for [bmim][BF4] and are largely independent of the incoming angle, whereas they strongly depend on the incident angle for [bmim][Tf2N]. For the latter liquid, less translational energy is lost and less energy is dumped to the surface at the larger incident angle. Furthermore, both the rigid-body rotational energy change $\langle \Delta T_{rot} \rangle$ and rotational quantum number $\langle J \rangle$ indicate that CO₂ coming off [bmim][Tf2N] is rotationally hotter than for [bmim][BF4]. Similar dependence of these variables on incident angle is seen for the two RTILs as for the translational energy transfer. While the average final rotational energy is uncorrelated with incoming angle in [bmim][BF4], CO₂ is rotationally more excited for larger incident angle in [bmim][Tf2N]. Lastly, we note that overall vibrational energy (which is initially governed by a classical Boltzman distribution) is lost upon scattering. The bending modes ν_2 lose the largest amount of energy when CO₂ collides with the [bmim][BF4] surface. However, both the bending and asymmetric stretch modes ν_2 and ν_3 lose a similar amount of energy when CO₂ scatters from the [bmim][Tf2N] surface. Here we caution that the vibrational energy transfer results are likely more sensitive to quantum effects than either rotational or translational energy transfer results, so the results are not
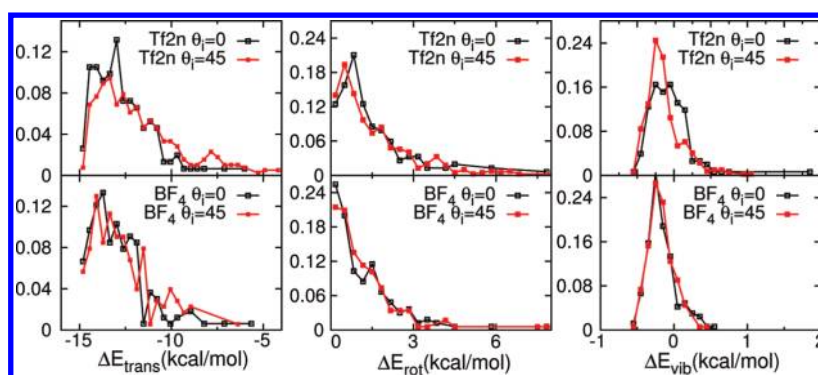
Figure 8. Probability distributions for energy transfer in translational, rotational, and vibrational degrees of freedom of outgoing CO_2 scattered off the surfaces of [bmim][BF4] and [bmim][Tf2N] at two different incident angles, $\theta_i = 0°$ and $\theta_i = 45°$.

expected to be accurate. We will therefore ignore vibrational energy transfer in the subsequent analysis.

3.3.1. Factors Governing the Difference between [bmim][BF4] and [bmim][Tf2N]. *Trajectories Characterized by Number of Collisions.* To decipher the critical factors responsible for the difference between [bmim][BF4] and [bmim][Tf2N] as described in the last section, we characterize the scattered trajectories based on the number of times that the CO_2 COM velocity changes its direction while colliding with the surface. Trapped trajectories are ignored. Qualitatively, trajectories with smaller collision numbers tend to escape the surface with more IS characteristics, while those with larger collision numbers are TD-like. We have empirically separated the single-collision dynamics from those with two or more collisions as a method for mechanistically decomposing the collision results. However, as noted in ref 69, a quantitative correspondence between the number of collisions and the experimental TD/IS fraction would require many more (and longer) trajectories to generate meaningful statistics. Both translational and rotational energy change have been analyzed based on collision number, as is presented in Table 5.

Table 5. Scattering Results Based on Number of Collisions

	[bmim][BF4]		[bmim][Tf2N]	
	$\theta_i = 0°$	$\theta_i = 45°$	$\theta_i = 0°$	$\theta_i = 45°$
total scattering probability	0.10	0.17	0.38	0.49
percentage with $N_{collision} = 1$[a,b]	58%	58%	58%	68%
percentage with $N_{collision} \geq 2$	42%	42%	42%	32%
$\langle \Delta T_{trans} \rangle$, $N_{collision} = 1$[c]	−12.4	−12.3	−12.0	−11.3
$\langle \Delta T_{trans} \rangle$, $N_{collision} \geq 2$	−13.5	−13.3	−13.2	−12.8
$\langle \Delta T_{rot} \rangle$, $N_{collision} = 1$	1.36	1.49	1.63	1.70
$\langle \Delta T_{rot} \rangle$, $N_{collision} \geq 2$	0.89	0.79	1.07	1.22

[a]Collision point is defined as the point where there is a change in the overall direction of motion along the surface normal. See descriptions in text. [b]With respect to the scattering trajectories. [c]Energy unit is kcal/mol.

In general, the fraction of trajectories for which CO_2 scatters off the surfaces through multiple contacts is higher in [bmim][BF4] compared to [bmim][Tf2N] at higher incident angle. This percentage is uncorrelated with the incident angle in [bmim][BF4], while a higher portion of CO_2 scatters through single-collision trajectories in [bmim][Tf2N] as the incident angle increases. We further notice that the incident angle has negligible effect on translational energy loss in [bmim][BF4]

regardless of the types of trajectories. However, less energy is lost at a 45° incident angle in [bmim][Tf2N]. For rotational excitation, the single-collision dynamics in [bmim][BF4] shows more energy at a larger incident angle, while this increase is reduced in [bmim][Tf2N]. This is in sharp contrast with multiple-collision dynamics. Compared to normal incidence, rotational energy gain is reduced in [bmim][BF4] at 45° incidence, while it is significantly enhanced for [bmim][Tf2N]. Compared to the results in Table 4, it is clear that the independence of final rotational energy on incident angle in [bmim][BF4] is the result of the reverse trend in rotational energy gain in single and multiple-collision dynamics. On the other hand, the significant rotational energy increase in [bmim][Tf2N] is caused by the considerable rise of the single-collision portion.

3.3.2. Analysis of Single-Collision-Type Trajectories. To further investigate the difference in dynamics between [bmim][BF4] and [bmim][Tf2N], the time evolution of the translational as well as rotational energy during the dynamics was monitored. The whole dynamics process is first divided into three stages as follows: (1) the "precollision" stage during which CO_2 approaches the surface, defined from the start of dynamics until 100 fs preceding the first collision point (where the CO_2 motion along the surface normal changes direction); (2) the "primary collision", when CO_2 strongly interacts with the surface, starting from the end of the precollision stage until 100 fs succeeding the first collision point in a single-collision trajectory and the last collision point in a multiple-collision trajectory; (3) the "postcollision", during which CO_2 exits the surface, which spans from the end of the primary collision until the end of the dynamics. The translational and rotational energy at the end of each stage was calculated and categorized according to the closest neighboring groups that CO_2 encounters. In addition, the average encountering probability of the various closest neighboring groups near CO_2 was collected as well. Results for single-collision and multiple-collision types are presented in Figures 9a and 12a, respectively. Finally, the dipole moment of CO_2, the minimum distance, and the final outgoing angle are also categorized based on the closest neighboring groups around CO_2 during the collisions, and averaged over all nontrapped trajectories. Figure 9b represents single-collision results, and Figure 12b is for multiple-collision results. We clarify that in all these figures, the normal incident data are represented using bars with crossing lines, while results for the 45° incident angle are denoted by solid filled bars. In Figures 9a and 12a, the translational and rotational energies for the three above-mentioned stages are clustered
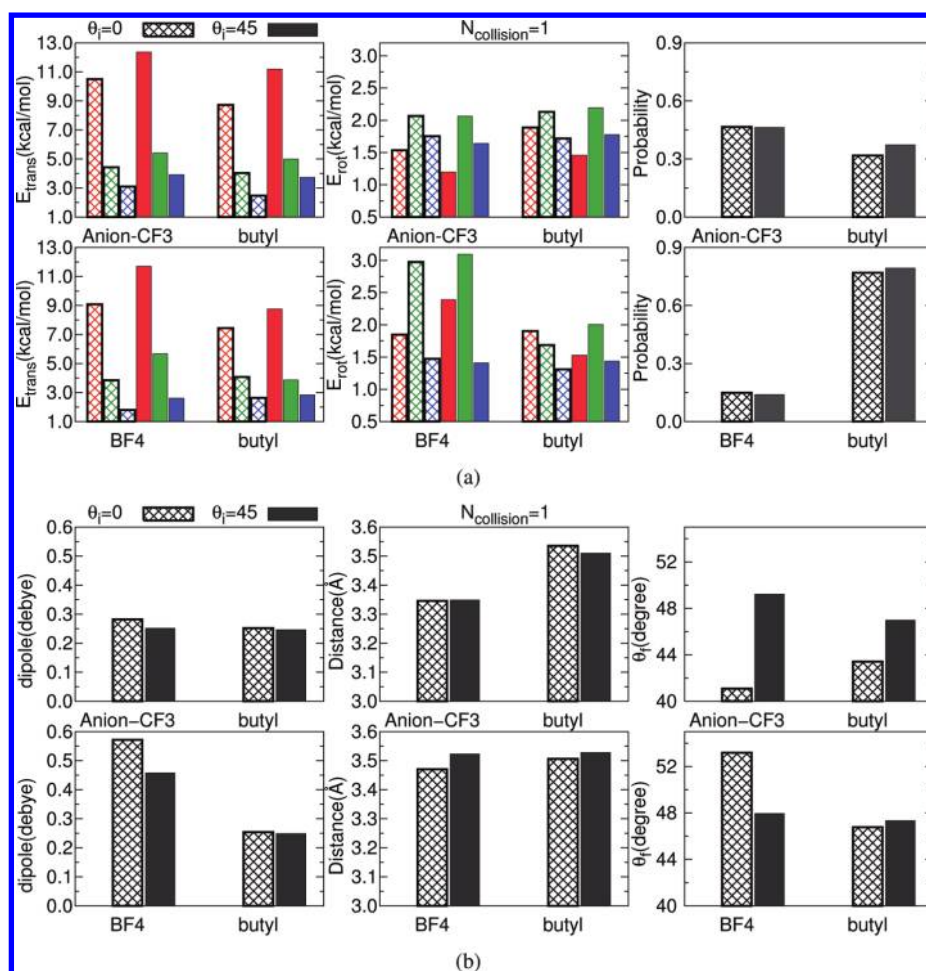
Figure 9. In part a, the top panels represent [bmim][Tf2N], while bottom ones are for [bmim][BF4]. From left to right: translational energy, rotational energy during different stages, and average encountering probability of the closest neighboring groups about CO_2. Bars filled with crossing lines and solid color are results for normal and 45° incident angle, respectively. Energies at different stages are clustered into groups of three from left-to-right, i.e., the bars with red, green, and blue colors represent precollision, primary collision, and postcollision stages, respectively. (b) Top: [bmim][Tf2N]; bottom: [bmim][BF4]. Left to right: average dipole moment, CO_2 distance, and final outgoing angle categorized according to the closest neighboring groups near CO_2. Shadowed and solid bars are results for normal and 45° angle incidence, respectively. Only groups with encountering probability of more than 0.05 are shown. Note that all results are from single-collision-type trajectories.

together and arranged left-to-right. The different stages are color-coded such that red, green, and blue depict the pre-collision, primary collision, and postcollision stages, respectively.

Translational Energy Transfer. From the single-collision results in Figure 9a, we first notice that the encountering probability, as expected, is consistent with the surface enhancement results in Section 3.1, as displayed in Figures 4 and 5. Namely, the surface of [bmim][BF4] is dominated by the butyl chain with only a minor contribution from the anion [BF4]. However, the surface of [bmim][Tf2N] is almost equally shared between the CF_3 and butyl-C4 groups. Second, in the case of [bmim][BF4], although CO_2 exits the surface after collision with the anion [BF4] with higher final translational energy (blue shadowed and solid bars on bottom left figure), and at larger incident angle compared to normal incidence, the final energy of CO_2 coming off the surface is dominated by the butyl chains, and is therefore insensitive to the incident angle. This is responsible for the rather weak correlation between translational energy transfer and the incident direction for the single-collision-type trajectories in

Table 5. By contrast, for the [bmim][Tf2N] surface, the trajectories encounter a surface that is enhanced in both anion-CF_3 and butyl groups so there is significantly higher translational energy at 45° incidence. Another feature worth noting is the differences in translational energy loss during the precollision stage (red shadowed and solid bars on bottom left). We see that energy loss during this stage is greater on the [bmim][BF4] surface, especially when CO_2 collides with the butyl chains. This, of course, is a direct manifestation of the rougher surface associated with [bmim][BF4] due to the protruding butyl chains as described in Section 3.1 (see Figures 4, 5, and 6). In addition, although a large portion of the energy left after the precollision stage (red to green bars) is subsequently lost in the primary collision stage, the postcollision process also leads to energy loss (green to blue bars), indicating that there are significant strong interactions between CO_2 and surface species while the CO_2 is exiting the surface. Particularly, this energy reduction is largest when CO_2 encounters the anion [BF4], which is consistent with the result that [BF4] binds CO_2 most strongly as in Section 2.2 and Figures 2 and 3 in Section 2.3. This strong binding also leads to

greater absorption as is confirmed by the potential of mean force (PMF) of CO_2 approaching the two surfaces as presented in Figure 10. The PMF, which is calculated using all our dynamics trajectories, is defined as[86]
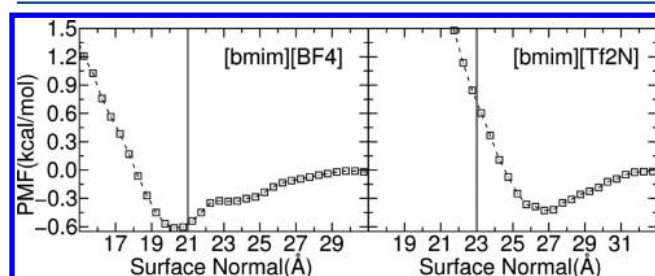

Figure 10. PMF of CO_2 approaching the surfaces of the two RTILs (a) [bmim][BF4] and (b) [bmim][Tf2N]. The gray lines represent the boundary between the maximum-density and surface regions as in Figure 4.

$$w(z) = \int_{z_0}^{z} -\nabla_{z'} w(z') \, dz'$$

$$= \int_{z_0}^{z} \frac{\int e^{-\beta U}(-\nabla_{z'} U) \, d\mathbf{r_{bath}}}{\int e^{-\beta U} \, d\mathbf{r_{bath}}} \, dz'$$

$$= \int_{z_0}^{z} -\overline{\nabla_{z'} U} \, d\mathbf{r_{bath}} \, dz' \tag{7}$$

where z and $\mathbf{r_{bath}}$ are the CO_2 COM z coordinate and the coordinates of the RTIL slab, respectively. Also, U and $-\nabla_{z'} U$ are the potential of the whole system and force along the surface normal acting on the COM of CO_2, respectively. Since the impact of CO_2 on the temperature of the slab is negligible throughout the dynamics, we have approximated the Boltzmann factor $e^{-\beta U}$ as a constant. The force $-\nabla_{z'} U$ is first binned according to the z coordinates to obtain the average force $-\nabla_{z'} U$ and then integrated to give the final PMF $w(z)$.

As shown in Figure 10, it is clear that both surfaces can be absorptive since minima are seen in the PMFs along the surface normal. Moreover, the minimum energy in [bmim][BF4] is 0.2 kcal/mol lower than that of [bmim][Tf2N]. This relative trend between the two RTILs agrees with the enthalpy of adsorption data[46] from CO_2 solubility measurements and recent simulations using polarizable models.[87] While the PMF minimum of [bmim][BF4] occurs deep in the maximum-density region, CO_2 tends to be absorbed in the surface region of [bmim][Tf2N] (gray lines). According to the reduced 1D number and mass density profiles in Figure 4, the number density of [BF4] anions starts to build up near the PMF minimum of [bmim][BF4] (~20 Å), and as a result, the higher surface adsorption energy in [bmim][BF4] is due to the higher binding energy of CO_2 with [BF4] as demonstrated in Section 2.3. On the other hand, the higher surface mass density of [bmim][Tf2N] due to the enhanced population of the larger anion at the surface (Figures 4, 5, and 6) prevents the CO_2 from penetrating further. Thus, the interplay of surface topology and binding energy of CO_2 with the anion is the primary reason for the differences in scattering probabilities and translational energy transfer between [bmim][BF4] and [bmim][Tf2N].

Features of the protruding butyl chains on the [bmim][BF4] surface are also evident in Figure 10, where a bump in the PMF

is noted in the region between 22 and 24 Å, which is missing in the smoother [bmim][Tf2N] surface.

Rotational Energy Transfer. The difference in the final rotational state can be analyzed similarly. As shown in Figure 9a, the final rotational energy of the carbon dioxide molecule coming off the [bmim][Tf2N] surface is higher than that of [bmim][BF4] (blue shadowed and solid bars in the middle panels) regardless of the identity of groups with which CO_2 collides. As shown in Table 5, the increase in final energy as a function of incident angle in [bmim][BF4] is directly traced to those trajectories where CO_2 clashes with butyl chains. Meanwhile, CO_2 ejected by either the anion-CF_3 groups or butyl chains leaves the [bmin][Tf2N] surface with similar energy at different incoming angles. Further inspection indicates that the rotational energy is increased when CO_2 approaches both surfaces during the precollision stage (red bars) at all incident angles. This increase is generally larger when CO_2 comes down on the [bmim][BF4] surface and less at larger incident angle for both RTILs. During the primary collision stage (red to green bars), the rotational energy continues to grow when CO_2 encounters the various groups; this increase is generally greater on the [bmim][Tf2N] surface compared to [bmim][BF4]. We also note that the increase in rotational energy of CO_2 upon collision with the anion [BF4] is much more dramatic than with other groups. Moreover, the energy that the CO_2 possesses at this stage is independent of the incident angle for [bmim][Tf2N]. Finally, during the postcollision stage when CO_2 exits the surface, the loss of rotational energy (green to blue bars) is more severe coming off the [bmim][BF4] surface. Thus, it is clear that the combination of significantly greater increase in rotational energy during primary collision and less decrease during postcollision is responsible for the higher final rotational energy of scattered CO_2 off the [bmim][Tf2N] surface. Since rotation is the direct result of torque exerted on CO_2, we have examined the anisotropy of the PMF associated with the orientation of CO_2 by providing a PMF for CO_2 approaching both surfaces of RTILs in head-on and flat configurations in Figure 11. The
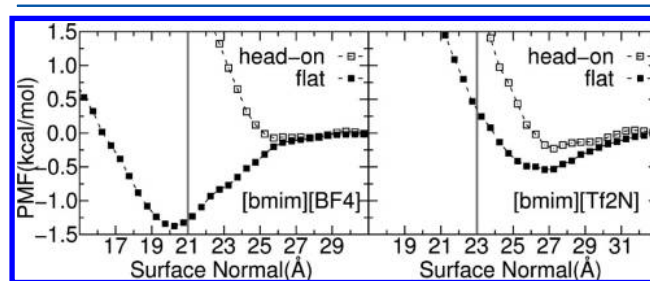

Figure 11. PMF of CO_2 approaching the surfaces of the two RTILs in head-on and flat orientations for (a) [bmim][BF4] and (b) [bmim][Tf2N]. Note that CO_2 is considered as head-on when the angle between the OO axis and the surface normal is in the range of $[0,30°]$ and flat when the angle between the OO axis and the xy-plane is in the interval of $[0,30°]$. The gray lines represent the boundary between the maximum-density and surface regions as in Figure 4.

orientation of CO_2 is considered as head-on when the angle between the OO axis and the surface normal is in the range of $[0,30°]$ and flat when the angle between the OO axis and the xy-plane is in the interval of $[0,30°]$.
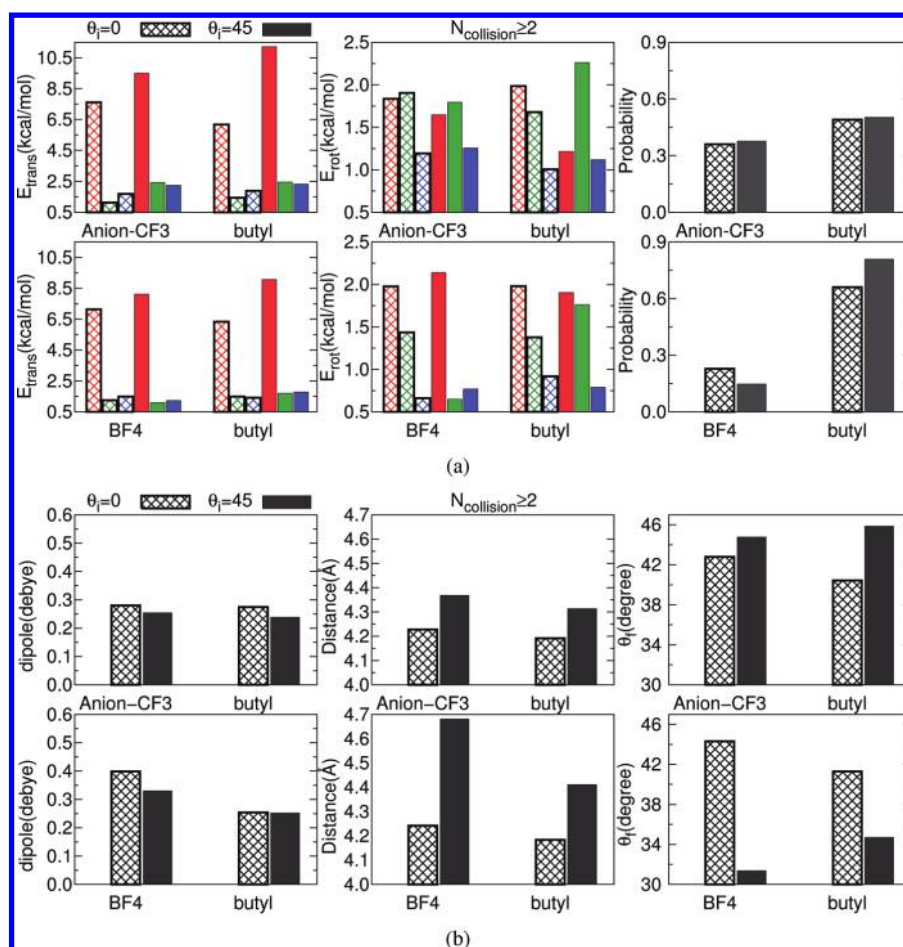
Figure 12. In part a, the top panels represent [bmim][Tf2N], while the bottom ones are for [bmim][BF4]. From left to right: translational energy, rotational energy during different stages, and average encountering probability of the closest neighboring groups to the CO_2. Bars filled with crossing lines and solid color are results for normal and 45° incidence, respectively. Energies at different stages are clustered into groups of three in left-to-right order, i.e., the bars with red, green, and blue colors represent precollision, primary collision, and postcollision stage, respectively. (b) Top: [bmim][Tf2N]; bottom: [bmim][BF4]. Left to right: average dipole moment, CO_2 distance, and final outgoing angle categorized according to the closest neighboring groups near CO_2. Shadowed and solid bars are results for normal and 45° incidence, respectively. Only groups with encountering probability of more than 0.05 are shown. Note that all results are from multiple-collision-type trajectories.

From Figure 11, it is evident that the greater increase in rotational energy during the precollision stage as CO_2 comes near the [bmim][BF4] surface, especially when CO_2 encounters the anion [BF4], is due to the larger degree of anisotropy of the PMF. This dependence of the PMF on CO_2 orientation is consistent with the cluster calculation presented in Figures 2 and 3. Since CO_2 prefers to be aligned parallel to the xy-plane, this torque rotates the CO_2 molecule as CO_2 approaches both surfaces. The higher torque gives CO_2 greater angular momentum on [bmim][BF4], especially when it comes near the anion [BF4]. However, the greater increase seems to be counterbalanced by two factors: (1) the greater anisotropy of the PMF, which increases rotation to a larger degree during precollision, is also more efficient at hindering rotation when CO_2 exits the surface. (2) CO_2 colliding with the rougher [bmim][BF4] surface tends to leave with a larger outgoing angle θ_f (right of Figure 9b). Hence, the probability of interacting with the protruding butyl chains during postcollision is increased, which reduces the rotational energy during the postcollision stage even more than in [bmim]-[Tf2N]. Hence, the interplay of surface topology and anisotropy of the binding curve associated with the relative

orientation of CO_2 is the primary reason for the difference in rotational distributions between [bmim][BF4] and [bmim]-[Tf2N].

Various experimental and theoretical studies have hinted at the strong interaction between CO_2 and anions in RTILs.[47,50,51] This feature is also evident in Figure 9b (left panels) in two ways: (1) CO_2 around anions in both RTILs possesses a larger induced dipole moment, especially when CO_2 collides with the smaller anion [BF4]. (2) the average distances between CO_2 and anions are shorter. Furthermore, the electronic polarization effect associated with CO_2 interacting with RTIL is often significant, as the CO_2 close to the anion-CF_3 and butyl chains possesses a significant induced dipole moment. Careful scrutiny indicates that the large induced dipole of CO_2 can be mostly attributed to the asymmetric charge distribution on the two oxygen atoms. This seems to confirm the presence of Lewis-type acid−base interactions between CO_2 and the RTILs.

3.3.3. Analysis of Multiple-Collision-Type Trajectories. In Figure 12a,b, we have provided information similar to that in Figure 9a,b for multiple-collision trajectories. In the right panels of Figure 12a, we notice that the distributions of the

encountering probability with various groups is different from those of single-collisions. Specifically, CO_2 interacts more often with the anion [BF4] on the [bmim][BF4] surface and with the butyl chains on the [bmim][Tf2N] surface. This is due to (1) the substantial interaction between CO_2 and the anion [BF4], as shown in Section 2.2 and Section 3.3.2, and (2) the shallower penetration of CO_2 into the [bmim][Tf2N] surface caused by larger translational energy reduction in the precollision stage (red bars on the left panels of Figure 12a). Also note in the left panels that the translational energy loss during the precollision stage is greater than that in the single-collision dynamics (red bars). Multiple clashes with both surfaces reduce the translational energy much more after primary collision (red to green bars) compared to single-collisions. The dependence of the final energy on the incident angle is similar to the single-collision type results. However, compared to the energy reduction from primary collision to postcollision stages in single-collision trajectories, this decline is almost negligible for multiple-collisions. This of course, can be traced to a smaller outgoing angle as shown in the right panels in Figure 12b, since smaller θ_f is likely to reduce the encountering probability of CO_2 with surface groups when it leaves the surfaces. For the rotational energy results, we see that CO_2 gains more energy during the precollision stage compared to the single-collision results since the smaller translational velocity increases the net torque exerted on CO_2. At the primary collision stage, unlike the single-collision results, multiple collisions are fairly efficient at hindering rotation, which is responsible for the much lower rotational energy seen in Table 5. Since CO_2 seems to reach thermal equilibrium with the surfaces after many collisions (average rotational energy at room temperature $T_{rot}^{298K} = 3kT/2 = 0.89$ kcal/mol), the effect of torque on the rotational energy is more stochastic. However, an exception is found at 45° incidence when CO_2 interacts more often with the butyl chains on the [bmim][Tf2N] surface, where collision increases the rotational energy substantially as in the single-collision dynamics. Since the much smoother [bmim][Tf2N] surface is unable to equilibrate the CO_2 rotationally (with much higher energy than thermal energy in Table 5), the scattered CO_2's tend to have more IS characteristics. Thus, surface roughness seems to play a bigger role in determining the rotational distribution than the anisotropy of the PMF in the multiple-collision dynamics. Figure 12b shows that the average distances between CO_2 and the neighboring groups are larger than those in single-collision type trajectories. Also, the electronic polarization of CO_2 is evident through the large induced dipole moment.

3.4. Scattering Results from MM Simulations and Comparison with Experiment.

MM Simulations. To investigate the influence of electronic polarization on the final scattering results, we have carried out simulations using a fixed point charge MM force field and compared the results with QM/MM data in previous sections. In these MM dynamics calculations, the initial conditions are identical with the QM/MM trajectories. Only normal incidence trajectories were considered. The results are summarized in Table 6.

The MM results show that the CO_2 has a much higher propensity to be inelastically scattered from the surfaces than in the QM/MM results (see Table 6). The increase is almost 4-fold for the [bmim][BF4] surface. Furthermore, compared to QM/MM results, the MM force field overestimates the portion of collisions in which CO_2 scatters off the surfaces through multiple collisions for both RTILs. Particularly, in

Table 6. Comparison of Scattering Results between QM/MM and MM Simulations[a]

	[bmim][BF4]		[bmim][Tf2N]	
	$\theta_i = 0°$			
	QM/MM	MM	QM/MM	MM
total scattering probability	0.10	0.38	0.38	0.59
percentage with $N_{collision} = 1$	58%	42%	58%	49%
percentage with $N_{collision} \geq 2$	42%	58%	42%	51%
$\langle \theta_{out} \rangle (°)$	44.9	41.8	41.7	43.4
$\langle \Delta T_{trans} \rangle$	−12.9	−13.3	−12.5	−12.9
$\langle \Delta T_{trans} \rangle, N_{collision} = 1$	−12.4	−12.7	−12.0	−12.2
$\langle \Delta T_{trans} \rangle, N_{collision} \geq 2$	−13.5	−13.7	−13.2	−13.5
$\langle \Delta T_{rot} \rangle$	1.16	0.89	1.40	1.06
$\langle \Delta T_{rot} \rangle, N_{collision} = 1$	1.36	1.05	1.63	1.26
$\langle \Delta T_{rot} \rangle, N_{collision} \geq 2$	0.89	0.78	1.07	0.86
$\langle \Delta T_{vib} \rangle$	−0.16	−0.16	−0.070	−0.19
$(|\langle \Delta E_{tot} \rangle|)/T_{init}$	0.78	0.83	0.74	0.79
$\langle J \rangle$	27	23	29	25

[a]For each RTIL, 800 trajectories were carried out using the MM force field. Initial conditions are identical with QM/MM dynamics.

contrast to the QM/MM results, more trajectories are identified as multiple-collision in the MM results for [bmim][BF4]. While the average outgoing angle from MM is reduced for collisions with [bmim][BF4], this number increases for [bmim][Tf2N].

In terms of energy transfer, it should be noted that the MM force field tends to be more efficient at reducing the translational energy, although this difference is only a few percent. On the other hand, in comparison with QM/MM, the MM force field greatly diminishes the rotational energy increase in both RTILs. In fact, the average rotational temperature of CO_2 coming out of both surfaces is fairly close to room temperature. Characterization of trajectories based on the number of collisions shows that while both single and multiple collision trajectories give less rotational excitation, this difference is greater for single-collision trajectories. Also, a larger portion of the total energy is transferred to the surface when the MM force field is used. In summary, it is evident that the MM force field is *more rigid* than QM/MM in the description of CO_2 collisions.

To probe this point in a more detailed fashion, plots identical to those in Figures 9 and 12 of the various properties of CO_2 during various stages of the collision as categorized according to the closest neighboring groups are provided in Figure 13a,b. These results are for single-collision-type trajectories. Note that MM and QM/MM results are displayed by bars filled with crossing lines and solid colors, respectively.

The results show that more translational energy is lost during precollision (red bars on left panels in Figure 13a) in the MM dynamics. Meanwhile, CO_2 is excited rotationally to a much greater degree during precollision. However, the higher energy during precollision is subsequently counterbalanced by a much larger decrease in the subsequent primary collision and postcollision stages.

The more rigid nature of the MM force field is directly related to electronic polarization of the CO_2, as is evident in Figure 13b. In dramatic contrast with the QM/MM results, the induced dipole moment in CO_2 is almost negligible. Moreover, the induced dipole moment in the MM calculations is independent of the identity of the neighboring groups.
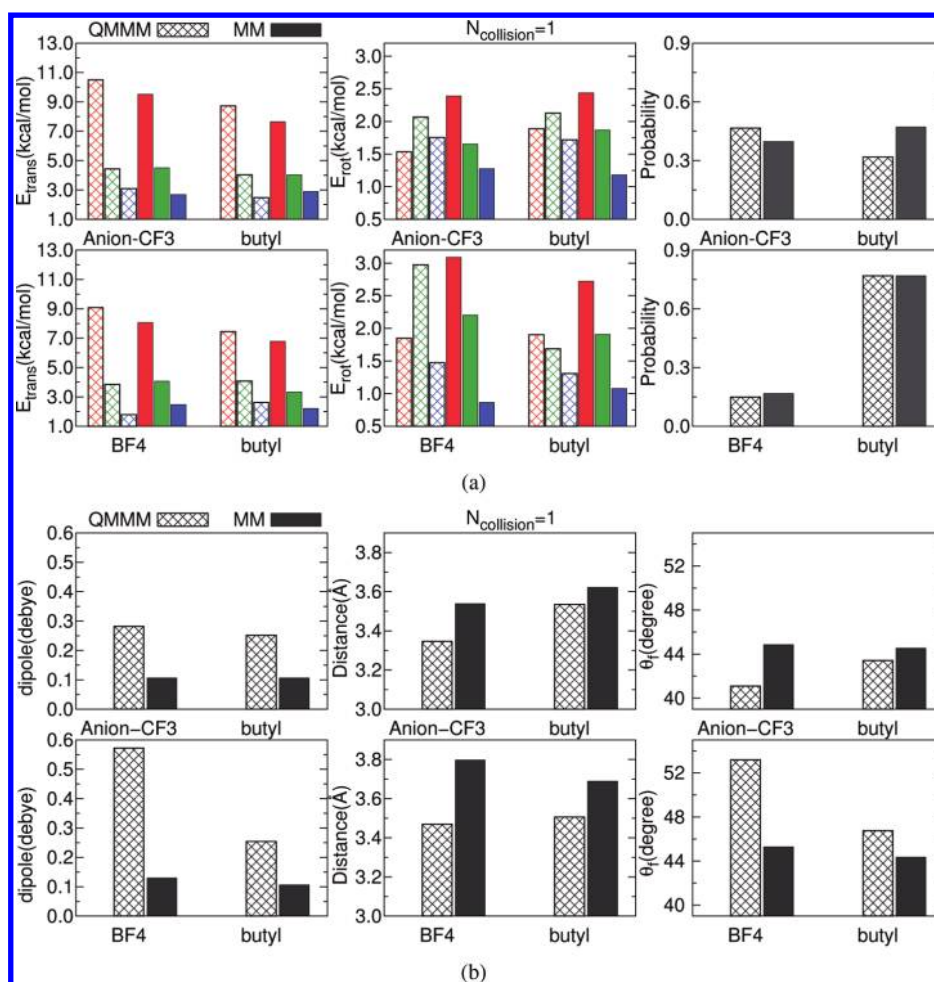
Figure 13. In part a, the top panels represent [bmim][Tf2N], while the bottom ones are for [bmim][BF4]. From left to right: translational energy, rotational energy during different stages, and average encountering probability of the closest neighboring groups about CO_2. Shadowed and solid bars are results using QM/MM and MM methods, respectively. Energies at different stages are clustered into groups of three in left-to-right order, i.e., the bars with red, green, and blue colors represent precollision, primary collision, and postcollision stages, respectively. (b) Top: [bmim][Tf2N]; bottom: [bmim][BF4]. Left to right: average dipole moment, CO_2 distance, and final outgoing angle categorized according to the closest neighboring groups near CO_2. Shadowed and solid bars are results for normal and 45° incidence, respectively. Only groups with encountering probabilities more than 0.05 were shown. Note that all results are from single-collision-type trajectories.

A consequence of the lack of electronic polarization is the much diminished interaction of CO_2 with the ions in RTILs. This is evident from the roughly 0.2−0.4 Å (middle panels of Figure 13b) larger average distances between CO_2 and neighboring groups in the MM dynamics compared to QM/MM.

Finally, we compare PMFs of CO_2 approaching the two RTILs surfaces obtained from the QM/MM and MM simulations. The results are presented in Figure 14. It should be noted first that the PMF minima from the MM simulations are fairly close in energy to those generated from the QM/MM calculations (left panels of Figure 14a,b). However, there are two critical differences for [bmim][BF4]: (1) the QM/MM minimum is deeper into the bulk, and (2) the QM/MM bump in the region [22, 24]Å due to the protruding butyl groups is missing in the MM result. These results are consistent with less absorption of CO_2 in the MM calculations, which is what is observed. By looking at the variation of PMF with the orientation of CO_2 (right panel of Figure 14a), we find that the MM results tend to overbind the head-on configuration, while binding of the flat orientations is underestimated. This is likely due to the lack of polarization, since the fixed negative charge

on oxygen in CO_2 favors interaction with the positive hydrogen on the terminal butyl chain and avoids the negative fluorine in [BF4] in the classical force field. The weaker anisotropy of the MM potential that results from these effects leads to lower rotational excitation in the trajectory results.

The QM/MM and MM PMFs obtained for [bmim][Tf2N] are fairly similar with both having minima that are farther out from the bulk region than for [bmim][BF4], as noted previously, and this explains the smaller CO_2 absorption that is found. However, the orientation-specific potentials show trends that are the opposite of what we saw for [bmim][BF4] with MM tending to under-bind the "head-on" configuration and the minimum moving inward for the flat configuration. One would imagine that the greater anisotropy of the MM potential would lead to more rotational excitation than QM/MM, but this is not found. However, except for this, our analysis provides a detailed picture concerning the importance of electronic polarization in determining the dynamical properties of the collisions.

Comparison with Experiment. We compare both QM/MM and MM results with the scattering experiments of Roscioli and
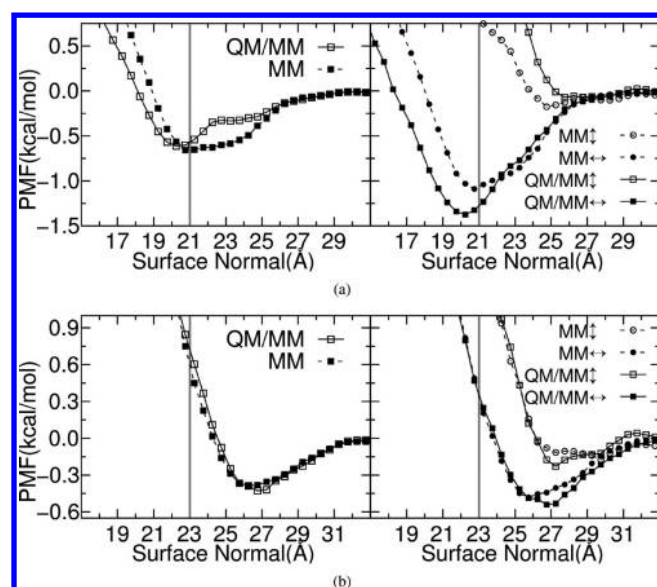
Figure 14. (a) Left panel: PMF of CO_2 approaching the [bmim][BF4] surface obtained from QM/MM and MM methods. Right panel: PMF of CO_2 approaching [bmim][BF4] surface with head-on (vertical double-headed arrow) and flat (horizontal double-headed arrow) orientations using QM/MM and MM approaches. (b) The same curves for CO_2 approaching [bmim][Tf2N] surface.

4. CONCLUSIONS

In this publication, QM/MM simulations using the PM6-DH:OPLS-AA level of theory have been carried out to model the scattering of hyperthermal CO_2 on surfaces of two common imidazolium-based RTILs, [bmim][BF4] and [bmim][Tf2N]. The semiempirical QM method PM6-DH was first benchmarked using cluster models, and it was found to show reasonable accuracy compared to both DFT B3LYP-D and post Hartree−Fock MP2 methods. Then we examined the RTIL surfaces using MM simulations with SBCs and found features in agreement with previous experimental and computational studies, with the smaller anion liquid, [bmim][BF4], completely dominated by the protruding butyl chains, while the bigger anion in [bmim][Tf2N] leads to roughly equal populations of the terminal anion-CF_3 group and flattened butyl chains.

Several conclusions have been made from the QM/MM scattering studies. First, the CO_2 is more easily absorbed into [bmim][BF4] than [bmim][Tf2N], and there is greater loss in translational energy and less rotational excitation in the CO_2s that inelastically scatter. These differences have been further analyzed by characterizing the trajectories according to the number of reversals in the CO_2 center of mass motion and by categorizing translational and rotational energy, encountering probability, induced dipole moment in CO_2, and distance between CO_2 and other neighboring groups during collision. These analyses clearly showed that the strong anion dependence of the final states of CO_2 is the result of complex interplay between energy transfer, absorption, and scattering that results from topological and interaction energy differences depending on anion identity. The PMF of CO_2 approaching the RTIL surfaces demonstrated that the adsorption energy of CO_2 in [bmim][BF4] is 0.2 kcal/mol higher than in [bmim][Tf2N]. The combination of higher adsorption energy and the rougher surface structure of [bmim][BF4] causes more efficient loss of CO_2 translational energy during collision, and favors adsorption. Meanwhile, the degree of anisotropy of the PMF favors larger torque in [bmim][BF4], but this is counterbalanced by the presence of protruding butyl chains which diminish rotational excitation when CO_2 exits the [bmim]-[BF4]. Thus, although the [bmim][Tf2N] surface is much smoother and less anisotropic, interaction of CO_2 with the surface leads to more rotational excitation in the scattered CO_2. Note that on both surfaces, there is a large induced dipole moment in CO_2 due to its interaction with neighboring groups. This is partly due to electronic polarization and is critical in determining the final rotational excitation of CO_2. Scattering dynamics from a fixed point charge force field thus shows much less rotational excitation on both RTILs. Finally, the TD trapping fraction and IS channel rotational temperature from QM/MM are in reasonable agreement with experiment, while

Nesbitt,[38] where the CO_2 TD fraction and the rotational temperature in the IS channel were determined from a two-process TD/IS model. The surface trapping fraction and IS rotational temperature were obtained by fitting our rotational quantum number J distribution to this model. We note that the fitting is constrained so as to reduce correlation between parameters. Results are summarized in Table 7.

It should be noted first that the trends in both the surface TD trapping fraction and IS rotational temperature between the two RTILs are reproduced in the QM/MM simulations. Also, the IS channel rotational temperatures of the two RTILs are in good agreement with experiment. On the other hand, although the trend in the TD trapping fraction and IS temperature is also correctly captured using MM results, the IS rotational temperatures from MM are uniformly much lower than those obtained from either QM/MM or experiment. From the previous discussion, this is caused by the lack of electronic polarization of CO_2 in the fixed point charge MM method. Our results therefore clearly indicate that any attempt to study the dynamical properties of CO_2 (i.e., gas uptake process) in RTIL excluding the polarization effect is likely to fail.

Table 7. Trapping Fraction and IS Channel Rotational Temperature from Fitting[a]

	MM[b]		QM/MM				experiment[c]	
	[BF4]	[Tf2N]	[BF4]		[Tf2N]		[BF4]	[Tf2N]
	$\theta_i = 0°$	$\theta_i = 0°$	$\theta_i = 0°$	$\theta_i = 45°$	$\theta_i = 0°$	$\theta_i = 45°$	$\theta_i = \theta_f = 45°$	$\theta_i = \theta_f = 45°$
α	0.50[d]	0.50[d]	0.55(3)	0.50[d]	0.50[d]	0.50[d]	0.74(1)	0.64(2)
T_{IS}(K)	410(11)	628(15)	798(15)	816(130)	981(199)	1099(110)	805(24)	908(45)

[a]Using a two-process TD/IS model. A constrained nonlinear least-squares fit was used, where α is constrained to be in [0.5, 1.0] and T_{IS} in [300, 2000] K. Results are fitted up to a maximum quantum number $J = 55$. Note that due to Bose−Einstein statistics of ^{16}O, only even J's were observed in ref 38. However, with classical nuclear dynamics and a limited number of scattering trajectories, especially in [bmim][BF4], we have included all odd and even J's in our fitting. [b]Same scattering conditions as in QM/MM simulations. [c]From ref 38. [d]Reaches the lower end of constraint.

the IS temperature in the MM results is much lower than the experimental findings. This discrepancy is caused by the lack of crucial electronic polarization of CO_2 in MM.

■ ASSOCIATED CONTENT

⑤ Supporting Information

MM parameters used for carbon dioxide and the time running average of surface tension of the two RTILs surfaces. This material is available free of charge via the Internet at http://pubs.acs.org.

■ AUTHOR INFORMATION

Corresponding Author

*E-mail: schatz@chem.northwestern.edu (G.C.S.); djn@jila.colorado.edu (D.J.N.).

Notes

The authors declare no competing financial interest.

■ ACKNOWLEDGMENTS

■ REFERENCES

(1) Petersen, M. K.; Iyengar, S. S.; Day, T. J. F.; Voth, G. A. *J. Phys. Chem. B* **2004**, *108*, 14804.

(2) Petersen, P. B.; Saykally, R. J. *Annu. Rev. Phys. Chem.* **2006**, *57*, 333.

(3) Buch, V.; Milet, A.; Vacha, R.; Jungwirth, P.; Devlin, J. P. *Proc. Natl. Acad. Sci. U.S.A* **2007**, *104*, 7342.

(4) Vacha, R.; Buch, V.; Milet, A.; Devlin, J. P.; Jungwirth, P. *Phys. Chem. Chem. Phys.* **2007**, *9*, 4736.

(5) Beattie, J. K. *Phys. Chem. Chem. Phys.* **2008**, *10*, 330.

(6) Vacha, R.; Buch, V.; Milet, A.; Devlind, J. P.; Jungwirth, P. *Phys. Chem. Chem. Phys.* **2008**, *10*, 332.

(7) Bhattacharyya, I.; Maze, J. T.; Ewing, G. E.; Jarrold, M. F. *J. Phys. Chem. A* **2010**, *115*, 5723.

(8) Holbrey, J. D.; Seddon, K. R. *Clean Prod. Processes* **1999**, *1*, 223.

(9) Welton, T. *Chem. Rev.* **1999**, *99*, 2071.

(10) Jutz, F.; Andanson, J.-M.; Baiker, A. *Chem. Rev.* **2011**, *111*, 322.

(11) Blanchard, L. A.; Hancu, D.; Beckman, E. J.; Brennecke, J. F. *Nature* **1999**, *399*, 28.

(12) Anderson, J. L.; Dixon, J. K.; Maginn, E. J.; Brennecke, J. F. *J. Phys. Chem. B* **2006**, *110*, 15059.

(13) Huang, J.; Riisager, A.; Wasserscheid, P.; Fehrmann, R. *Chem. Commun.* **2006**, *38*, 4027.

(14) *Material Matters*; Aldrich Chemical Co, Inc: Milwaukee, WI, 2007; Vol. 2, No. 2.

(15) Giridhar, P.; Venkatesan, K.; Srinivasan, T.; Rao, P. V. *Electrochim. Acta* **2007**, *52*, 3006.

(16) Swatloski, R. P.; Spear, S. K.; Holbrey, J. D.; Rogers, R. D. *J. Am. Chem. Soc.* **2002**, *124*, 4974.

(17) He, P.; Liu, H.; Li, Z.; Liu, Y.; Xu, X.; Li, J. *Langmuir* **2004**, *20*, 10260.

(18) Wu, B. Novel ionic liquid thermal storage for solar thermal electric power systems. In *Proceedings of the Solar Forum*; Washington, D.C., 2001.

(19) Chambreau, S. D.; Schneider, S.; Rosander, M.; Hawkins, T.; Gallegos, C. J.; Pastewait, M. F.; Vaghjiani, G. L. *J. Phys. Chem. A* **2008**, *112*, 7816.

(20) He, L.; Tao, G.-H.; Parrish, D. A.; Shreeve, J. M. *Chem.—Eur. J.* **2010**, *16*, 5736.

(21) Gao, H.; Ye, C.; Gupta, O. D.; Xiao, J.-C.; Hiskey, M. A.; Twamley, B.; Shreeve, J. M. *Chem.—Eur. J.* **2007**, *13*, 3853.

(22) He, L.; Tao, G.-H.; Parrish, D. A.; Shreeve, J. M. *Chem.—Eur. J.* **2010**, *16*, 5736.

(23) Schneider, S.; Hawkins, T.; Rosander, M.; Vaghjiani, G.; Chambreau, S.; Drake, G. *Energy Fuels* **2008**, *22*, 2871.

(24) Iimori, T.; Iwahashi, T.; Kanai, K.; Seki, K.; Sung, J.; Kim, D.; Hamaguchi, H.-o; Ouchi, Y. *J. Phys. Chem. B* **2007**, *111*, 4860.

(25) Iimori, T.; Iwahashi, T.; Ishii, H.; Seki, K.; Ouchi, Y.; Ozawa, R.; o. Hamaguchi, H.; Kim, D. *Chem. Phys. Lett.* **2004**, *389*, 321.

(26) Sung, J.; Jeon, Y.; Kim, D.; Iwahashi, T.; Iimori, T.; Seki, K.; Ouchi, Y. *Chem. Phys. Lett.* **2005**, *406*, 495.

(27) Iwahashi, T.; Miyamae, T.; Kanai, K.; Seki, K.; Kim, D.; Ouchi, Y. *J. Phys. Chem. B* **2008**, *112*, 11936.

(28) Sung, J.; Jeon, Y.; Kim, D.; Iwahashi, T.; Seki, K.; Iimori, T.; Ouchi, Y. *Colloids Surf., A* **2006**, *284 - 285*, 84.

(29) Petersen, P. B.; Saykally, R. J. *J. Phys. Chem. B* **2005**, *109*, 7976.

(30) Rivera-Rubero, S.; Baldelli, S. *J. Phys. Chem. B* **2006**, *110*, 15499.

(31) Santos, C. S.; Rivera-Rubero, S.; Dibrov, S.; Baldelli, S. *J. Phys. Chem. C* **2007**, *111*, 7682.

(32) Aliaga, C.; Baldelli, S. *J. Phys. Chem. B* **2007**, *111*, 9733.

(33) Rivera-Rubero, S.; Baldelli, S. *J. Phys. Chem. B* **2006**, *110*, 4756.

(34) Santos, C. S.; Baldelli, S. *J. Phys. Chem. B* **2007**, *111*, 4715.

(35) Gannon, T. J.; Law, G.; Watson, P. R.; Carmichael, A. J.; Seddon, K. R. *Langmuir* **1999**, *15*, 8429.

(36) (a) Saecker, M. E.; Nathanson, G. M. *J . Chem. Phys.* **1993**, *99*, 7056. (b) Nathanson, G. M.; Davidovits, P.; Worsnop, D. R.; Kolb, C. E. *J. Phys. Chem.* **1996**, *100*, 13007. (c) Saecker, M. E.; Govoni, S. T.; Kowalski, D. V.; King, M. E.; Nathanson, G. M. *Science* **1991**, *252*, 1421. (d) Krebs, T.; Nathanson, G. M. *J. Phys. Chem. A* **2011**, *115*, 6317. (e) Zhang, J.; Lahankar, S. A.; Garton, D. J.; Minton, T. K.; Zhang, W.; Yang, X. *J. Phys. Chem. A* **2011**, *115*, 10894. (f) Wu, B.; Zhang, J.; Minton, T. K.; McKendrick, K. G.; Slattery, J. M.; Yockel, S.; Schatz, G. C. *J. Phys. Chem. C* **2010**, *114*, 4015. (g) Waring, C.; King, K. L.; Costen, M. L.; McKendrick, K. G. *J. Phys. Chem. A* **2011**, *115*, 7210. (h) Perkins, B. G. Jr.; Nesbitt, D. J. *Phys. Chem. Chem. Phys.* **2010**, *12*, 14294. (i) Perkins, B. G. Jr.; Nesbitt, D. J. *Proc. Natl. Acad. Sci. U.S.A.* **2008**, *105*, 12684. (j) Perkins, B. G. Jr.; Nesbitt, D. J. *J. Phys. Chem. B* **2008**, *112*, 507. (k) Perkins, B. G. Jr.; Nesbitt, D. J. *J. Phys. Chem. A* **2007**, *111*, 7420. (l) Perkins, B. G. Jr.; Nesbitt, D. J. *J. Phys. Chem. B* **2006**, *110*, 17126. (m) Perkins, B.; Haber, T.; Nesbitt, D. *J. Phys. Chem. B* **2005**, *109*, 16396.

(37) Roscioli, J. R.; Nesbitt, D. J. *J. Phys. Chem. A* **2011**, *115*, 9764.

(38) Roscioli, J. R.; Nesbitt, D. J. *J. Phys. Chem. Lett.* **2010**, *1*, 674.

(39) Lynden-Bell, R. M.; Kohanoff, J.; Popolo, M. G. D. *Faraday Discuss.* **2005**, *129*, 57.

(40) Lynden-Bell, R. M. *Mol. Phys.* **2003**, *101*, 2625.

(41) Lynden-Bell, R. M.; Popolo, M. D. *Phys. Chem. Chem. Phys.* **2006**, *8*, 949.

(42) Pinilla, C.; Pópolo, M. G. D.; Lynden-Bell, R. M.; Kohanoff, J. *J. Phys. Chem. B* **2005**, *109*, 17922.

(43) Bhargava, B. L.; Balasubramanian, S. *J. Am. Chem. Soc.* **2006**, *128*, 10073.

(44) Yan, T.; Li, S.; Jiang, W.; Gao, X.; Xiang, B.; Voth, G. A. *J. Phys. Chem. B* **2006**, *110*, 1800.

(45) Pensado, A. S.; Malfreyt, P.; Pádua, A. A. H. *J. Phys. Chem. B* **2009**, *113*, 14708.

(46) Anthony, J. L.; Anderson, J. L.; Maginn, E. J.; Brennecke, J. F. *J. Phys. Chem. B* **2005**, *109*, 6366.

(47) Kazarian, S. G.; Briscoea, B. J.; Weltonb, T. *Chem. Commun.* **2000**, *2000*, 2047.

(48) Cadena, C.; Anthony, J. L.; Shah, J. K.; Morrow, T. I.; Brennecke, J. F.; Maginn, E. J. *Phys. Chem. Chem. Phys.* **2004**, *126*, 5300.

(49) Perez-Blanco, M. E.; Maginn, E. J. *J. Phys. Chem. B* **2010**, *114*, 11827.

(50) Bhargava, B. L.; Balasubramanian, S. *Chem. Phys. Lett.* **2007**, *444*, 242.

(51) Prasad, B. R.; Senapati, S. *J. Phys. Chem. B* **2009**, *113*, 4739.

(52) Bhargava, B. L.; Balasubramanian, S. *J. Phys. Chem. B* **2007**, *111*, 4477.

(53) Stewart, J. *J. Mol. Model.* **2007**, *13*, 1173.

(54) Rezac, J.; Fanfrlik, J.; Salahub, D.; Hobza, P. *J. Chem. Theory Comput.* **2009**, *5*, 1749.

(55) Korth, M. *J. Chem. Theory Comput.* **2010**, *6*, 3808.

(56) Berendsen, H. J. C.; Postma, J. P. M; van Gunsteren, W. F.; DiNola, A.; Haak, J. R. *J. Chem. Phys.* **1984**, *81*, 3684.

(57) Nosé, S. *J. Chem. Phys.* **1984**, *81*, 511.

(58) Nosé, S. *Mol. Phys.* **1984**, *52*, 255.

(59) Martyna, G. J.; Tuckerman, M. E.; Tobias, D. J.; Klein, M. L. *Mol. Phys.* **1996**, *87*, 1117.

(60) (a) Lopes, J. N. C.; Deschamps, J.; Padua, A. A. H. *J. Phys. Chem. B* **2004**, *108*, 2038. (b) Lopes, J. N. C.; Padua, A. A. H. *J. Phys. Chem. B* **2004**, *108*, 16893. (c) Lopes, J. N. C.; Padua, A. A. H. *J. Phys. Chem. B* **2006**, *110*, 19586. (d) Lopes, J. N. C.; Padua, A. A. H.; Shimizu, K. *J. Phys. Chem. B* **2008**, *112*, 5039. (e) Shimizu, K.; Almantariotis, D.; Gomes, M. F. C.; Padua, A. A. H.; Lopes, J. N. C. *J. Phys. Chem. B* **2010**, *114*, 3592.

(61) Stoppa, A.; Hunger, J.; Buchner, R. *J. Chem. Eng. Data* **2009**, *54*, 472.

(62) Harris, K. R.; Kanakubo, M.; Woolf, L. A. *J. Chem. Eng. Data* **2007**, *52*, 1080.

(63) Hess, B.; Kutzner, C.; van der Spoel, D.; Lindahl, E. *J. Chem. Theory Comput.* **2008**, *4*, 435.

(64) Bakowies, D.; Thiel, W. *J. Phys. Chem.* **1996**, *100*, 10580.

(65) Swope, W. C.; Andersen, H. C.; Berens, P. H.; Wilson, K. R. *J. Chem. Phys.* **1982**, *76*, 637.

(66) Tuckerman, M.; Berne, B. J.; Martyna, G. J. *J. Chem. Phys.* **1992**, *97*, 1990.

(67) Stewart, J. P. *MOPAC2009*. Stewart Computational Chemistry, version 11.053L.

(68) Harris, J. G.; Yung, K. H. *J. Phys. Chem.* **1995**, *99*, 12021.

(69) Martinez-Nunez, E.; Rahaman, A.; Hase, W. L. *J. Phys. Chem. C* **2007**, *111*, 354.

(70) Grimme, S.; Antony, J.; Ehrlich, S.; Krieg, H. *J. Chem. Phys.* **2010**, *132*, 154104.

(71) Neese, F. *ORCA*, version 2.8-20. Lehrstuhl für Theoretische Chemie Wegelerstr. 12D-53115 Bonn, Germany.

(72) A. Schaefer, H. H.; Ahlrichs, R. *J. Chem. Phys.* **1992**, *97*, 2571.

(73) Weigenda, F.; Ahlrichs, R. *Phys. Chem. Chem. Phys.* **2005**, *7*, 3297.

(74) Krishnan, R.; Binkley, J. S.; Seeger, R.; Pople, J. A. *J. Chem. Phys.* **1980**, *72*, 650.

(75) Kendall, R. A.; Fruchtl, H. A. *Theor. Chem. Acc.* **1997**, *97*, 158.

(76) Eichkorn, K.; Weigend, F.; Treutler, O.; Ahlrichs, R. *Theor. Chem. Acc.* **1997**, *97*, 119.

(77) a. Eichkorn, K.; Treutler, O.; Ohm, H.; iser, M. H.; Ahlrichs, R. *Chem. Phys. Lett.* **1995**, *240*, 283.

(78) Whitten, J. L. *J. Chem. Phys.* **1973**, *58*, 4496.

(79) Neese, F.; Wennmohs, F.; Hansen, A.; Becker, U. *Chem. Phys.* **2009**, *356*, 98.

(80) Ohno, A.; Hashimoto, H.; Nakajima, K.; Suzuki, M.; Kimuraa, K. *J. Chem. Phys.* **2009**, *130*, 204705.

(81) Sloutskin, E.; Ocko, B. M.; Tamam, L.; Kuzmenko, I.; Gog, T.; Deutsch, M. *J. Phys.: Condens. Matter* **2005**, *127*, 7796.

(82) Law, G.; Watson, P. R. *Langmuir* **2001**, *17*, 6138.

(83) Wandschneider, A.; Lehmann, J. K.; Heintz, A. *J. Chem. Eng. Data* **2008**, *53*, 596.

(84) Li, X.; Moore, D. T.; Iyengar, S. S. *J. Chem. Phys.* **2008**, *128*, 184308.

(85) Li, X.; Oomens, J.; Eyler, J. R.; Moore, D. T.; Iyengar, S. S. *J. Chem. Phys.* **2010**, *132*, 244301.

(86) McQuarrie, D. A. *Statistical Mechanics*, 1st ed.; University Science Books: Sausalito, CA, 2000.

(87) Dang, L. X.; Chang, T.-M. *J. Phys. Chem. Lett.* **2012**, *3*, 175.